Eur. Phys. J. D **9**, 95–104 (1999)

THE EUROPEAN PHYSICAL JOURNAL D

EDP Sciences

Structures and spectra of gold nanoclusters and quantum dot molecules

R.N. Barnett, C.L. Cleveland, H. Häkkinen, W.D. Luedtke, C. Yannouleas, and U. Landman

School of Physics, Georgia Institute of Technology, Atlanta, GA 30332-0430, USA

Received: 1 September 1998 / Received in final form: 15 December 1998

Abstract. Size-evolutions of structural and spectral properties in two types of finite systems are discussed. First we focus on energetics and structures of gold clusters, particularly Au_N in the $40 \lesssim N \lesssim 200$ range exhibiting a discrete sequence of optimal clusters with a decahedral structural motiff, and on the electronic structure of bare and methyl-thiol passivated Au_{38} clusters. Subsequently, bonding and spectra of quantum dot molecules (QDM's) are investigated, using a single-particle two-center oscillator model and the local-spin-density (LSD) method, for a broad range of interdot distances and coupling strengths. A molecular orbital classification of the QDM states correlates between the united-dot and separated-dots limits. LSD addition energies and spin polarization patterns for QDM's in the entire coupling range are analyzed, guiding the construction of a constant interaction model. A generalization of the non-interacting-electrons Darwin–Fock model to QDM's is presented. Wigner crystallization of the electrons leading to formation of Wigner supermolecules is explored in both the field-free case and with a magnetic field using a spin-and-space unrestricted Hartree–Fock method.

PACS. 36.40.Cg Electronic and magnetic properties of clusters – 73.20.Dx Electron states in low-dimensional structures (superlattices, quantum well structures and multilayers)

1 Introduction

That the properties of materials depend on their size and form of aggregation is commonly expected and often observed, and research aimed at understanding the systematics and origins of such size-evolutionary patterns is a main theme in cluster science [1]. Unlike the behavior of bulk matter where properties often scale with size, the dependence of materials properties on size when some (or all) of the physical dimensions are reduced is often of discrete and non-monotonic nature. Such is the case for finite clusters (termed zero-dimensional, 0D), for ultra-thin wires (quasi one-dimensional, 1D), and for ultra-thin (2D) films or a thin layer of electrons, as well as 0D quantum dots, confined at a heterostructural interface (e.g., in GaAs/AlGaAs). Examples of the discrete non-monotonic nature of the variation of the properties of such systems with their size (expressed in terms of the number of elementary constituents, i.e., electrons and atoms) and of size evolutionary patterns include: the occurrence of magic number sequences in clusters, originating from electronic- and/or atomic (packing)-shell effects [1–4]; electronic shell effects portrayed in addition energy spectra of 2D quantum dots ("artificial atoms") [5–7]; and electronic transport, energetics and structural characteristics of metallic nanowires [8, 9], including the occurrence of cluster-derived structures [10], conductance quantization [9] and magic radii sequences [11].

While research pertaining to the physical properties of naturally occurring finite materials systems (e.g., atomic and molecular aggregates) has by now nearly matured, forming an area commonly referred to as "cluster science", studies of 0D artificially fabricated structures (often called "quantum dots") are more recent, beginning in the early 1980's. Common to both finite materials aggregates (e.g., metal and semiconductor clusters) and artificial dots is the quantization of the electrons' motion due to confinement, leading to frequent reference to the latter as "artificial atoms" [5, 6]. Note, however, the different relevant length and energy scales in the two systems, with the Fermi wavelength and Fermi energy in typical metal clusters being $\sim 0.5\,\text{nm}$ and $\sim 5\,\text{eV}$, while the corresponding values in semiconductor heterostructures (e.g., GaAs/AlGaAs) are $\sim 50\,\text{nm}$ and $10\,\text{meV}$, respectively, necessitating (in the latter) measurements under cryogenic conditions. Moreover, in artificial quantum dots the charge carriers are confined through electrical gating and/or etching techniques applied to a two-dimensional electron gas, with the capability of varying and controlling the dot's size and shape. On the other hand, the development of methods of preparation and isolation of materials clusters with well defined sizes and geometrical structures is more complex, requiring understanding of the energetics of cohesion and binding in materials clusters (metals in particular), as well as identification and elucidation of the physical principles underlying self-selection

of "magic" sequences of sizes and structural motifs in these systems.

In light of the above, we focus on two systems which serve to illustrate some of the issues which are the subject of current research in this area. First we discuss gold nanoclusters [12] (which may serve as an example of real materials quantum dots) [13] emphasizing aspects pertaining to their structural evolution and spectra, and subsequently we explore the electronic spectra of artificial (created by gate voltages) [5] quantum dots and lateral quantum dot molecules (QDM).

2 Structural evolution of gold nanocrystals

Nanometer size metal and semiconductor particles have been the subject of recent intensive experimental and theoretical research efforts aiming at their (size) controlled preparation and characterization and at an understanding of their properties and their size dependencies, in anticipation of the potential use of particles in this size range in optoelectronics, nanodevices, catalysis, and sensor technologies. Here we focus on gold nanoclusters which, as has been shown recently [12(a,b,d),14], can be obtained through controlled decomposition of gold-thiol molecules AuSR (R is an n-alkyl group) in the presence of excess RSSR molecules, which act as a passivant as well as etching agents. Most significant is the observation that in the size range most pertinent to this study (that is, Au_N with $N \lesssim 200$) well-controlled growth and subsequent separation results in essentially quantitative conversion of atomically dispersed gold into several distinct fractions of molecularly defined substances (rather than a continuum of sizes and structures) with cluster sizes corresponding to (gold) core masses near $8\,k$, $14\,k$, $22\,k$, and $28\,k$ ($k = 1000$ amu, or 5.08 Au atoms; i.e., expressed in terms of the number of atoms, these isolated fractions consist of thiol passivated gold clusters with gold cores of 40, 70, 110, and 140 atoms, respectively). These observations are in agreement with our theoretical predictions obtained through explorations of the atomistic energetics and structural motifs of Au_N clusters.

In the extensive structural survey, performed through energy-minimization of atomistic models with many-body embedded-atom (EAM) interactions [12(a,b,d)], we included a broad range of structural forms, guided by actual observations (mainly high-resolution electron microscopy and X-ray diffraction) as well as by past experience [15]. These studies have shown that the structural size-evolution in gold may be described as a sequence of transitions; (i) first from specific "molecular" structures, at the extremely small size range, with equivalent cluster diameter $d_{eq} < 1$ nm (< 30 atoms), to (ii) ordered "noncrystallographic" (in particular Marks decahedra [15,16], m−Dh) structures (here we use this term for motifs which do not occur in bulk crystals, e.g., fivefold symmetric ones) at larger sizes, and then culminating for sizes with $d_{eq} > 2$ nm (250 atoms), in (iii) crystallites of bulk lattice structure (fcc) with specific faceted

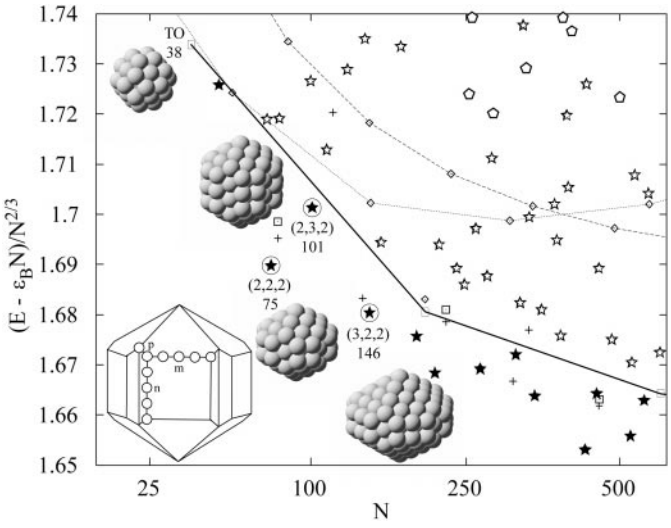

Fig. 1. Energies of structurally optimized Au_N ($N \leq 520$) clusters plotted as $(E - \varepsilon_B N)/N^{2/3}$ versus N (on an $N^{1/3}$ scale), where $\varepsilon_B = 3.93$ eV is the cohesive energy of an atom in bulk Au. Various structural motifs are denoted as: Oh (open diamond connected by long-dashed line); Ih (open diamond connected by dotted line); TO (solid diamonds); t-TO (open diamonds); TO^+ (+); t−TO^+ (open squares); i−Dh (open pentagons); and m−Dh (solid stars), with the filled stars denoting m−Dh clusters in the enhanced stability region. The 75, 101 and 146 atom m−Dh clusters corresponding to the stable structural sequence are denoted by encircled solid stars, and their structures, as well as that of Au_{38}, are shown. The (m, n, p) indices of m−Dh are shown in the inset, for a $(5, 5, 2)$ cluster.

morphologies (i.e., truncated octahedra, TO, variants thereof, TO^+, and their twins, t−TO). Since the first regime has been commonly discussed in the cluster literature [17] and the "convergence" to the bulk structure for large clusters (iii) was described by us in some detail elsewhere [12(a,b)], we focus here on the intermediate regime (ii) which is also the least "intuitive" and harder to resolve [12(d)].

Because of their discrete nature, atomistic models of various structural motifs and morphologies correspond to specific size (number-of-atoms) sequences. For example, the number of atoms in m-Dh decahedral crystallites can be expressed as $N = 1/6\{30p^3 - 135p^2 + 207p - 102 + [5m^3 + (30p - 45)m^2 + (60(p^2 - 3p) + 136)m] + n[15m^2 + (60p - 75)m + 3(10p^2 - 30p) + 66]\} - 1$, with m, n, and p as defined in Fig. 1 (bottom left inset). Examination of the energetics of the various structural motifs (Fig. 1) leads to identification of the energy-optimal pattern ("magic number" sequence). This procedure predicts that m−Dh clusters and fcc TO clusters (and their TO^+ and twinned variants) form the dominant size-sequences for Au_N. Furthermore, except in the very small size-range, the icosahedral (Ih) motif is found to be energetically non-competitive (due to accumulated icosahedral strain which grows with volume [15]), fcc clusters with octahedral (Oh) and cubeoctahedral (CO) morphologies are also noncompetitive with energies of the latter lying above the scale of the figure, and the competition between the fcc-TO motif and the

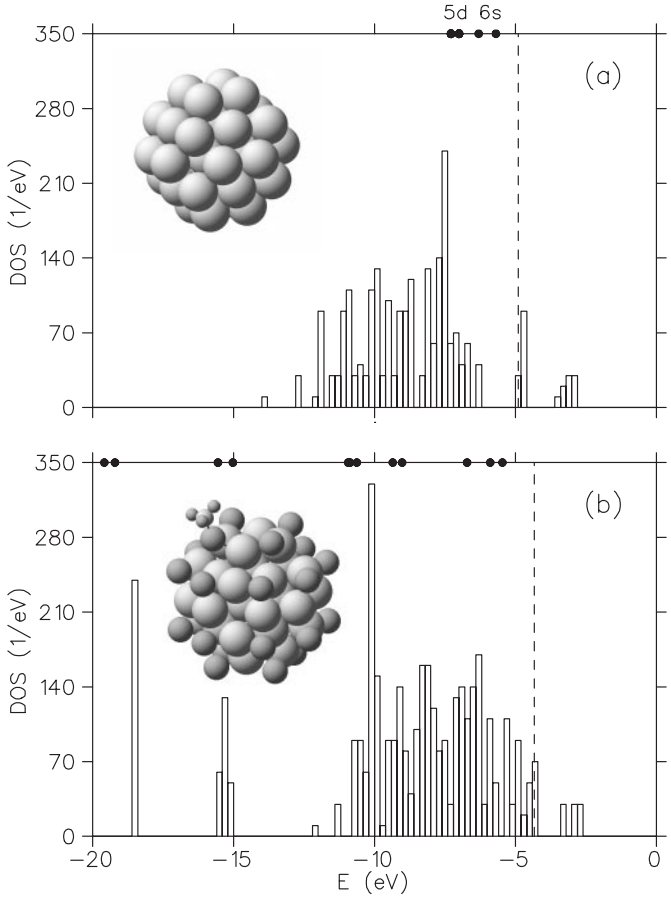

Fig. 2. Density of (Kohn–Sham) states (DOS) for optimized (a) Au_{38} cluster, and (b) $Au_{38}(SCH_3)_{24}$ cluster [structures shown in insets, with only the gold and sulfur (darker spheres) atoms and one of the CH_3 groups shown in (b)]. The atomic valence eigenvalues of Au are marked with filled dots in (a) and those for SCH_3 in (b). The dashed vertical lines denote the Fermi energy. The width of the energy bins is 0.2 eV.

Dh one maintains throughout, with the Dh advantage somewhat diminishing for larger clusters (due to accumulated volume dependent decahedral strain, which is smaller than the icosahedral one [15]). In the size range of interest to us here ($50 < N \lesssim 200$), the lowest-energy cluster sequence is made of Au_{75}, Au_{101} and Au_{146} all belonging to the m−Dh motif, with the (m, n, p) indices as indicated in Fig. 1 (see circled stars), and in very close correspondence with the mass-spectrometrically estimated core-masses of the fractionated samples used in the XRD measurements.

Furthermore, analyses of X-ray diffraction (XRD) intensity patterns measured for powder samples of each of the well separated (14 *k*, 22 *k*, and 28 *k*) fractions using a "first principles" mode of analysis [12(b,d),18] have shown that the above predicted sequence of clusters yields the best agreement with the data, to the exclusion of alternative ones [in each case, the theoretical result is not changed when the number of atoms is reduced by two, corresponding to removal of the top and bottom vertex atoms of the m−Dh (see Fig. 1)]

Consequently, we conclude from the above analysis that for gold the 1 nm $\lesssim d_{eq} \lesssim$ 2 nm size-range is punctuated by the formation of a discrete sequence of primarily three cluster sizes with m-Dh structues, thus providing an energetic and structural explanation for the observed preferential formation of this discrete sequence of stable gold nanocrystallites in this size range.

Having discussed above structural issues pertaining to gold clusters, we turn now to examination of their electronic properties with reference to charging characteristics, in light of their use as quantum dots and recent electrochemical charging experiments [13]. In particular, we focus on the smallest cluster shown in Fig. 1, that is Au_{38} (corresponding to the $\sim$ 8000 amu experimentally separated gold core-mass fraction [14(b)]). The optimal structure for this cluster calculated with the use of the EAM potentials is fcc with a TO morphology (Fig. 1). The electronic density of states (DOS) for the Au_{38} cluster, calculated via the local density functional (LDA) theory, with the use of nonlocal norm-conserving relativistic pseudopotentials [19, 20] (s, p, and d, with s taken as local and a plane wave kinetic energy cutoff of 62 Ry) is shown in Fig. 2(a), along with the structure of the cluster which has been further relaxed using the Hellmann–Feynman forces via the method described in [21]. The DOS of Au_{38} exhibits a three-fold degenerate HOMO state (6 states including spin, with 2 holes) due to the octahedral symmetry. Furthermore, there is a set of 18 empty states (including spin) just above the Fermi level, and gaps of 1.3 eV and 1.1 eV below and above the Fermi level, respectively. The orbital characters of the HOMO show significant s, p, and d hybridization. We note here that the total width of the valence band (9 eV) already corresponds closely to that of bulk fcc Au [22], although the finite size of the cluster leads to opening of a gap below the Fermi energy (bulk Au has a very low DOS in that region).

Passivation of the Au_{38} cluster was simulated by symmetrically positioning 24 methylthiol (SCH_3) molecules on the (111) facets close to the (100) edges; the choice of thiol-molecules to gold-atoms ratio (24/38) was guided by results from X-ray photoelectron spectroscopy measured for a separated fraction of gold-hexamethylthiol with a gold core-mass of $\sim$ 8000 amu [23]. The optimized LDA structure is shown in Fig. 2(b) together with the corresponding DOS. In the relaxed structure, the average interatomic distances in the gold crystallite are somewhat larger (2.95 Å – 2.97 Å) in the passivated cluster compared to 2.74 Å – 2.78 Å in the bare one, and the 8 atoms in the middle of the (111) facets are relaxed inwards with respect to the facet edges.

The most prominent features in the DOS of the passivated $Au_{38}(SCH)_{24}$ cluster are: (i) the two narrow "bands" at about −18.5 and −15.2 eV, formed from the SCH_3 molecular orbitals; (ii) the gold states are shifted up by 1.8 eV; (iii) the filling of the gap below the Fermi energy, and (iv) the significant reduction of electron holes at, and just above, the Fermi energy (the number of empty states including spin reduces to 6). The gap above the Fermi level is 0.9 eV. There is still a three-fold degenerate HOMO state, and a spatial analysis of it's orbital charge density reveals that it is concentrated around the outermost 24 gold atoms

and the surrounding 24 sulfur atoms, having d-character on the gold and p-character on the sulfurs. Furthermore, we find that the passivation of the cluster is accompanied by charge transfer from the Au_{38} core crystallite to the passivating molecules (total amount of close to 2 electrons).

In light of recent solution-phase electrochemical ensemble Coulomb staircase measurements on butane-thiol passivated Au_{38} clusters [13], we evaluated the addition energy ($\Delta\varepsilon$, see section III) which may be expressed as $\Delta\varepsilon = E(N_e+1) - 2E(N_e) + E(N_e-1) = \delta\varepsilon + e^2/C$, where N_e is the number of electrons and $\delta\varepsilon = \varepsilon(N_e+1) - \varepsilon(N_e)$ is the change in the single-electron energy of the highest occupied level, and the charging energy e^2/C defines the effective capacitance. Calculations for $N_e = N_e^0 \pm 1$ (where $N_e = N_e^0$ is the number of electrons in the neutral passivated cluster), and noting that when changing the charge on the cluster from -2 to $+2$ the added electron fills the holes in the degenerate set of levels (i.e., $\delta\varepsilon \approx 0$ and thus $\Delta\varepsilon$ yields the charging energy), resulted in an effective capacitance of ~ 0.085 aF, which compares well with the experimentally estimated value (0.13 aF); the difference between the two values may be accounted for by the longer chain thiols used in the experiments and the local polarization effects around the cluster in solution which would tend to increase the effective capacitance. Further details pertaining to these studies may be found elsewhere [24].

3 Quantum dots and dot molecules

While in the previous section we focussed on certain energetic and structural issues pertaining to natural materials' clusters, we turn now to a discussion of (artificial) quantum dots (QD's) created in semiconductor heterostructures, containing a (small) adjustable number of electrons (controlled by gate voltages). Recent measurements on such systems revealed a remarkable similarity between their spectra (e.g., shell structure) and that of naturally occurring zero-dimensional fermionic systems (e.g., atoms, nuclei, and clusters) suggesting the naming of these solid-state structures as "artificial atoms" [5,6], with potential utilization in electronics and computer technologies. Moreover, most recently several investigations have been made toward extending such an analogy to "artificial quantum dot molecules" (QDM's) [5,25] and artificial "quantum dot clusters", as well as, "artificial crystals" comprised of coupled quantum dots.

Theoretical investigations of the electronic structure of single QD's are rather abundant including: non-interacting single-electron (SE) treatments (Darwin–Fock model [26] for two-dimensional (2D) harmonically confined electrons in the presence of a magnetic field); self-consistent methods, i.e., Hartree, restricted and unrestricted Hartree–Fock [27] (HF and UHF, respectively), spin-and-space unrestricted Hartree–Fock (sS-UHF) [28], and local density functional methods [29] (LDA, LSD, and current-LSD); and exact diagonalization studies [27(a),30] (limited to a small number of electrons, typically less than 10). On the other hand, systematic understanding of the electronic spectra of lateral QDM's [28] (with and without external magnetic fields), bridging the weakly-coupled dots (tunnel-split) regime and the strong-coupling (covalent) one, as well as analogies between QDM's and their natural counterpart as a function of interdot distance, coupling strength, and magnetic field, is largely lacking.

Following the course of development for single QD's, first insights into the energetics and spectra of lateral QDM's may be gained from single-electron (SE) energy levels calculated for harmonic confinements using a semi-analytic two-center oscillator model (TCOM). Indeed, SE spectra, particularly in conjunction with a constant interaction model (CIM) generalized to include electron spin effects (Hund's rule), have proven most useful in the interpretation of transport measurements [addition energies (AE)] on single QDs [5,7]. In the absence of such detailed data for QDM (particularly in the strong interdot coupling regime), we use first, for magnetic-field-free situations, our LSD calculations, where electron-electron interactions and spin effects are treated self-consistently, as data for calibration of a SE-CIM spectrum and for assessment of the role of electronic screening on the (external) harmonic confinement potential (see, however, our discussion toward the end of this section, pertaining to self-consistent treatments of interacting electrons in QD's and QDM's).

In the TCOM, the single-particle levels associated with the artificial molecule, at both the strong (close to the united quantum dots, UQD) and weak coupling (close to the separated quantum dots, SQD) regimes, are determined by the single-particle hamiltonian [31]

$$H = T + \frac{1}{2}m^*\omega_{xi}^2 x^2 + \frac{1}{2}m^*\omega_{yi}^2 y_i'^2 + V_{\rm neck}(y) + h_i + \frac{g^*\mu_B}{\hbar}\mathbf{B}\cdot\mathbf{S}, \quad (1)$$

where $y_i' = y - y_i$ with $i = 1$ for $y < 0$ (left) and $i = 2$ for $y > 0$ (right), and the h_i's control the relative well-depth, thus allowing studies of hetero-QDM's (in the following, we limit ourselves to cases with $h_1 = h_2 = 0$). x denotes the coordinate perpendicular to the interdot axis (y). $T = (\mathbf{p} - e\mathbf{A}/c)^2/2m^*$, with $\mathbf{A} = 0.5(-By, Bx, 0)$, and the last term in (1) is the Zeeman interaction with g^* being the effective g factor and μ_B the Bohr magneton. Here we limit ourselves to systems with $\hbar\omega_{x1} = \hbar\omega_{x2} = \hbar\omega_x$. The most general shapes described by H are two semiellipses connected by a smooth neck [$V_{\rm neck}(y)$]. $y_1 < 0$ and $y_2 > 0$ are the centers of these semiellipses, $d = y_2 - y_1$ is the interdot distance, and m^* is the effective electron mass.

For the smooth neck, we use $V_{\rm neck}(y) = \frac{1}{2}m^*\omega_{yi}^2[c_i y_i'^3 + d_i y_i'^4]\theta(|y| - |y_i|)$, where $\theta(u) = 0$ for $u > 0$ and $\theta(u) = 1$ for $u < 0$. The four constants c_i and d_i can be expressed via two parameters, as follows: $(-1)^i c_i = (2 - 4\epsilon_i^{\rm b})/y_i$ and $d_i = (1 - 3\epsilon_i^{\rm b})/y_i^2$, where the barrier-control parameters $\epsilon_i^{\rm b} = (V_{\rm b} - h_i)/V_{0i}$ are related to the actual (controlable) height of the barrier ($V_{\rm b}$) between the two QD's, and $V_{0i} = m^*\omega_{yi}^2 y_i^2/2$ (for $h_1 = h_2$, $V_{01} = V_{02} = V_0$).

The single-particle levels of H, including an external perpendicular magnetic field B, are obtained by numerical

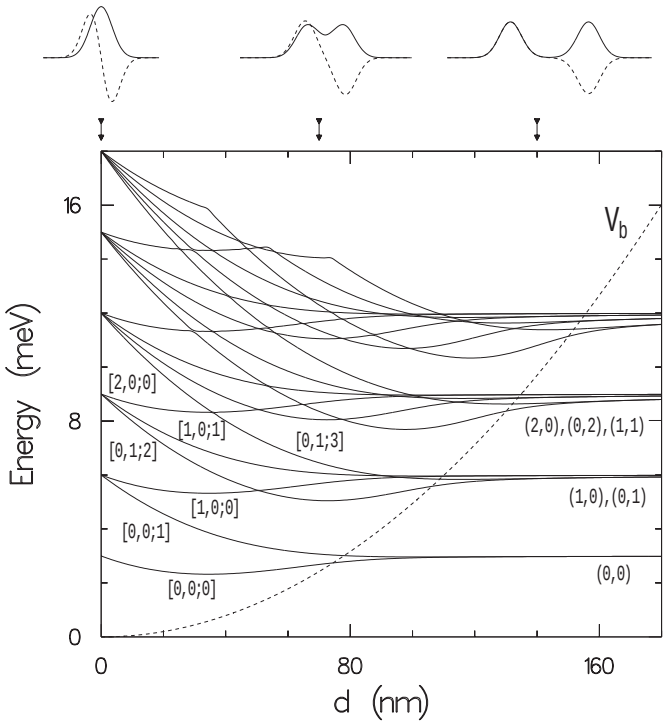

Fig. 3. SE spectra of QDM's plotted versus the distance d between two (identical) coupled QD's with TCOM confinement $\hbar\omega_{y1} = \hbar\omega_{y2} = \hbar\omega_x = 3\,\text{meV}$ and $h_1 = h_2 = 0$. For all d's the barrier control parameters were taken as $\epsilon_1^{\text{b}} = \epsilon_2^{\text{b}} = 0.5$, i.e., the barrier height (depicted by the dashed line) varies as $V_{\text{b}}(d) = V_0(d)/2$. MO's correlating the united ($V_{\text{b}} = 0$) and separated-dots limits are denoted along with the corresponding (on the right) SQD states. Wavefunction cuts at $x = 0$ along the y-axis at several distances d (see arrows) corresponding to the lowest bonding and antibonding eigenvalues (solid and dashed lines) are displayed at the top. Energies in meV and distances in nm.

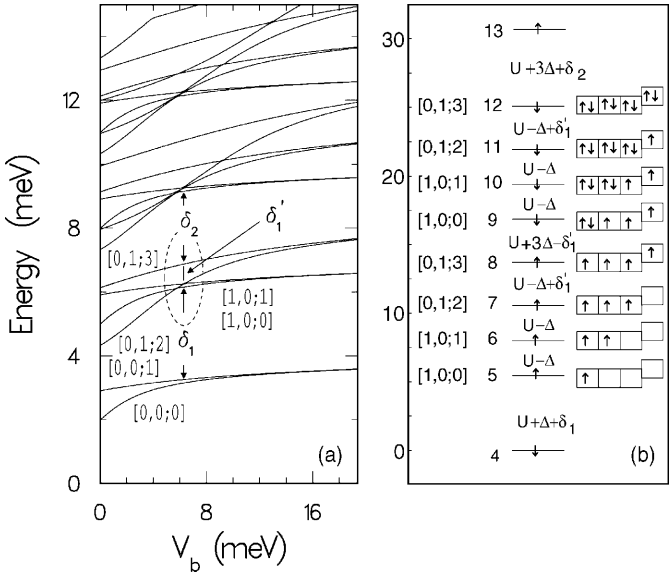

Fig. 4. (a) SE spectra of a QDM at $d = 70\,\text{nm}$ plotted versus the barrier height V_{b}. (b) CIM for the electrochemical potential in the region marked in (a); the value for $N = 4$ is taken as 0. With $U = 2.85\,\text{meV}$ and $\Delta = 0.35\,\text{meV}$ for the "charging" and Hund's exchange energies, and with the energy spacings $\delta_1 = 2.9\,\text{meV}$, $\delta_1' = 0.6\,\text{meV}$, and $\delta_2 = 2.1\,\text{meV}$ taken from the SE spectrum in (a), the CIM AE spectrum (given by the separations between the lines) and the associated spin polarization pattern ($N\uparrow - N\downarrow$, see boxes) agree rather well with the LSD results [see the AE spectrum ($4 \le N \le 12$) for the QDM with $V_{\text{b}}^{\text{bare}} = 10\,\text{meV}$ in Fig. 3].

diagonalization in a (variable-with-separation) basis consisting of the eigenstates of the auxiliary hamiltonian:

$$H_0 = \frac{\mathbf{p}^2}{2m^*} + \frac{1}{2}m^*\omega_x^2 x^2 + \frac{1}{2}m^*\omega_{yi}^2 y_i'^2 + h_i\,. \qquad (2)$$

This eigenvalue problem is separable in x and y, i.e., the wave functions are written as $\Phi_{m\nu}(x,y) = X_m(x)Y_\nu(y)$. The solutions for $X_m(x)$ are those of a one-dimensional oscillator, and for $Y_\nu(y)$ they can be expressed through the parabolic cylinder functions [31] $U[\alpha_i, (-1)^i\xi_i]$, where $\xi_i = y_i'\sqrt{2m^*\omega_{yi}/\hbar}$, $\alpha_i = (-E_y + h_i)/(\hbar\omega_{yi})$, and $E_y = (\nu + 0.5)\hbar\omega_{y1} + h_1$ denotes the y-eigenvalues. The matching conditions at $y = 0$ for the left and right domains yield the y-eigenvalues and the eigenfunctions $Y_\nu(y)$ (m is integer and ν is in general real).

The TCOM single-particle spectrum for a QDM made of two coupled (identical) QDs (with $\hbar\omega_x = \hbar\omega_{y1} = \hbar\omega_{y2} = 3\,\text{meV}$), plotted versus the distance, d, between the centers of the two dots, is given in Fig. 3. In these calculations the height of the barrier between the dots varies as a function of d, thus simulating reduced coupling between them as they are separated; we take the barrier control parameter $\epsilon_1^{\text{b}} = \epsilon_2^{\text{b}} = 0.5$. In all our calculations, we used GaAs values, $m^* = 0.067m_{\text{e}}$ and a dielectric constant $\kappa = 12.9$; the scaled units which we use are $2\,\text{Ry}^* = m^*e^4/\hbar^2\kappa^2 = 10.96\,\text{meV}$ and $\text{a}_{\text{B}}^* = \hbar^2\kappa/m^*e^2 = 10.188\,\text{nm}$. For the SQD (large d) and the UQD ($d = 0$) limits the spectra are the same, corresponding to that of a 2D harmonic oscillator (two of them for the SQD) with a level degeneracy of 1, 2, 3, ... In analogy with real molecules, the states in the intermediate region ($d > 0$) may be interpreted as molecular orbitals (MO's) made of linear superpositions of the states of the two dots comprising the QDM. This description is intuitively appealing, though it is more appropriate for the weaker coupling regime (large d); nevertheless we continue to use it for the whole range of coupling strength between the dots, including the strong coupling regime where reference to the states of the individual dots is only approximate. Thus, for example, as the two dots approach each other, the lowest levels (n_x, n_y) with $n_x = n_y = 0$ on the two dots may combine symmetrically ("bonding") or antisymmetrically ("antibonding") to form [0,0;0] and [0,0;1] MOs, with the third index denoting the total number of nodes of the MO along the interdot axis (y), that is, $2n_y + I$, $I = 0$ or 1; for symmetric combinations ($I = 0$) this index is even and for antisymmetric ones ($I = 1$) it is odd. Between the SQD and UQD limits the degeneracies of the individual dots' states are lifted, and in correlating these two limits the number of y-nodes is conserved; for example the [0,0;1] MO converts in the UD limit into the

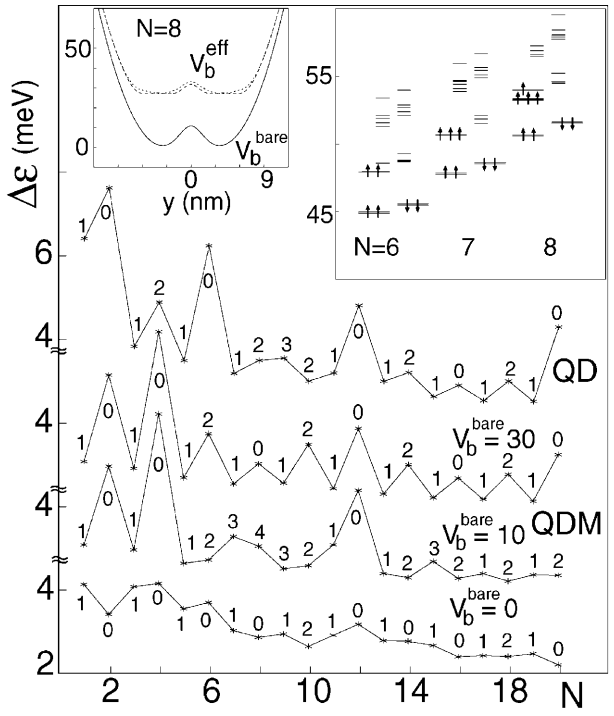

Fig. 5. LSD addition energy spectra for a single QD (with bare harmonic confinement parameters $\hbar\omega_x = \hbar\omega_y = 5$ meV, $\hbar\omega_z = 45$ meV) and for three QDM's at $d = 70$ nm with the same bare confinement parameters as above and $\hbar\omega_{y1} = \hbar\omega_{y2} = 5$ meV, for differing interdot barriers $V_{\rm b}^{\rm bare} = 0$, 10, and 30 meV. The spin polarizations $N\uparrow - N\downarrow$ are denoted on the curves. In the QDM's with $V_{\rm b}^{\rm bare} = 0$, 10 and 30 meV, for $N = 2$, the singlet states (0) correspond to electrons localized in the left and right wells of the QDM's (see also [28]). For both the circular single QD and the QDM's (particularly with $V_{\rm b}^{\rm bare} = 30$ meV), we find several deviations from Hund's rule. For example, for the single QD, the ground-state with $N = 16$ exhibits no spin polarization and corresponds to a spin-density wave [29(c)]. Left inset: the bare ($V^{\rm bare}$) and screened ($V^{\rm eff}$, given for both up and down electrons) potentials for the QDM ($d = 70$ nm and $V_{\rm b}^{\rm bare} = 10$ meV) with $N = 8$. Right inset: KS-LSD eigenvalues for $N = 6$, 7, and 8 for the QDM ($d = 70$ nm, $V_{\rm b}^{\rm bare} = 10$ meV); for each N, both the up and down spin manifolds are shown.

(0,1) state of a single QD, the [0,1;2] MO into the (0,2) state, and the [1,0;1] MO into the (1,1) state (see Fig. 3). Note that MOs of different symmetries may cross while they do not if they are of the same symmetry. The evolution of the $d = 70$ nm QDM spectrum as a function of $V_{\rm b}$ displayed in Fig. 4 (a), shows that the level spectrum with $V_{\rm b} = 0$, corresponding to a large non-circular dot, converges as the coupling is decreased (i.e., increasing $V_{\rm b}$) into that of two separated dots; note however that even for large $V_{\rm b}$ the 2D harmonic oscillator spectrum is not recovered because of the unharmonicity introduced by the interdot barrier.

Effects due to electron-electron interactions (including exchange-correlation) are revealed via our LSD calculations. The Kohn–Sham (KS)-LSD equations were solved [32] for 3D external (bare) harmonic confining potentials, with the frequencies $\hbar\omega_x = \hbar\omega_{y1} = \hbar\omega_{y2} = 5$ meV (in the plane of the dots) and $\hbar\omega_z = 45$ meV in the direction normal to the xy plane. The choice of these frequencies for the bare confinement was guided by previous studies [29(a,b)] which showed that one of the effects of interelectron interactions is to screen the bare-confinement potentials, and that the value of $\hbar\omega_z$ (45 meV) is sufficiently large to assure that for fillings of a single QD with at least up to 20 electrons they occupy only the lowest subband corresponding to the perpendicular (z) confinement [29(b)].

Significant screening of the bare confining potentials and a significant reduction of the bare barrier height ($V_{\rm b}^{\rm bare}$) are observed for the QDM. This effect is particularly strong for dots with $N > 4$ (see inset in Fig. 5 for $V_{\rm b}^{\rm bare} = 10$ meV, $N = 8$); using for the $d = 70$ nm QDM a bare barrier height of 10 meV (with this value chosen in order to obtain inter-level spacings of 3–4 meV in the QDM LSD calculations) yields self-consistent effective barriers ($V_{\rm b}^{\rm eff}$) of 11.68 meV, 10.26 meV, 8.06 meV, 6.16 meV, 5.17 meV and 4.77 meV for $N = 1-6$, respectively, and $V_{\rm b}^{\rm eff} \sim 4.5$ meV for $N > 6$.

Results of our calculations for the addition energies $\Delta\varepsilon = \mu(N+1) - \mu(N)$, where $\mu(N)$ is the electro-chemical potential [that is the total energy difference $\mu(N) = E_{\rm T}(N) - E_{\rm T}(N-1)$], for a single QD, and for the QDM at $d = 70$ nm with $V_{\rm b}^{\rm bare} = 0$, 10, and 30 meV, are shown in Fig. 5. In all cases clear signatures of electronic shell effects (termed also "magic numbers" in nuclear and atomic cluster physics) are evident [33] (see sequence of peaks in Fig. 5), with certain differences in the $\Delta\varepsilon$ patterns between the various cases (note e.g., peaks at $N = 7-8$ and $N = 15$ for the $V_{\rm b}^{\rm bare} = 10$ meV QDM, and the odd-even alternation for $V_{\rm b}^{\rm bare} = 0$). Particularly noted are differences in the spin-polarizations ($\Delta s = N_\uparrow - N_\downarrow$, denoted on the curves in Fig. 5), which reflect the influence of exchange interactions (Hund's rule). These trends in the QDM spectrum can be understood from inspection of the corresponding KS-LSD level schemes (see inset in Fig. 5) and the SE spectra (Fig. 3). For example for the QDM ($d = 70$ nm, $V_{\rm b}^{\rm bare} = 10$ meV) with $N = 1-4$, $V_{\rm b}^{\rm eff}$ varies between 11.68 meV and 6.16 meV. For this range of barrier heights the bonding and antibonding MO made of the (0,0) QD states are nearly degenerate and well separated from the other MOs (also see Fig. 4), and thus Hund's rule for $N = 1-4$ gives, respectively, the following filling pattern: $[0,0;0]^1$, $[0,0;0]^1[0,0;1]^1$, $[0,0;0]^2[0,0;1]$, and $[0,0;0]^2[0,0;1]^2$ (with the upper index outside the bracket denoting the occupancy). On the other hand for $N > 4$ $V_{\rm b}^{\rm eff}$ is smaller (varying from 5.17 for $N = 6$ to 4.01 meV for $N = 10$) and in this range of barrier heights the higher set of MOs [made out of the (1,0) and (0,1) QD states] are close to each other (with the [0,1;3] somewhat split-off, see Figs. 3 and 5, which correlates with the local maximum in $\Delta\varepsilon$ for $N = 7$, see Fig. 5) and they are separated from the higher MOs. Again, Hund's rule yields the filling pattern ("4" denotes the $N = 4$ "core"): "4"$[1,0;0]^1$, "4"$[1,0;0]^1[0,1;2]^1$, "4"$[1,0;0]^1[0,1;2]^1[1,0;1]^1$, "4"$[1,0;0]^1[0,1;2]^1[1,0;1]^1[0,1;2]^1$, and "4"$[1,0;0]^2[0,1;2]^1$ $[1,0;1]^1[0,1;3]^1$ for $N = 5-9$, with $\Delta s = 1, 2, 3, 4, 3$, respectively.

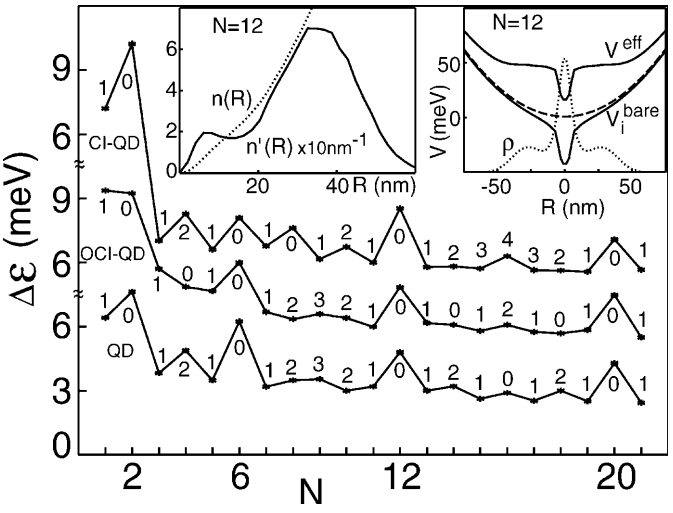

Fig. 6. Adiition energy spectra for a "clean" QD (bottom) and for two "dirty" dots with a hydrogenic impurity located at the center of the dot (CI-QD) and off-center (OCI-CD) at a distance of 17.5 a_b^* from the middle of the dot. The numbers above the points on the curves give the spin polarization $\Delta s = N\uparrow - N\downarrow$. In the right inset, the bottom solid line corresponds to the bare potential with the impurity ($V_i^{\rm bare}$), the long dashed line gives the bare harmonic confinement, the upper solid line corresponds to the LSD calculated effective potential ($V^{\rm eff}$), and the dotted line gives the electronic density (ρ) along a line passing through the middle of the CI-QD with $N = 12$ electrons. The integrated $[n(R)]$ and differential $[n'(R)]$ electronic densities for the CI-QD with $N = 12$ are displayed in the left inset.

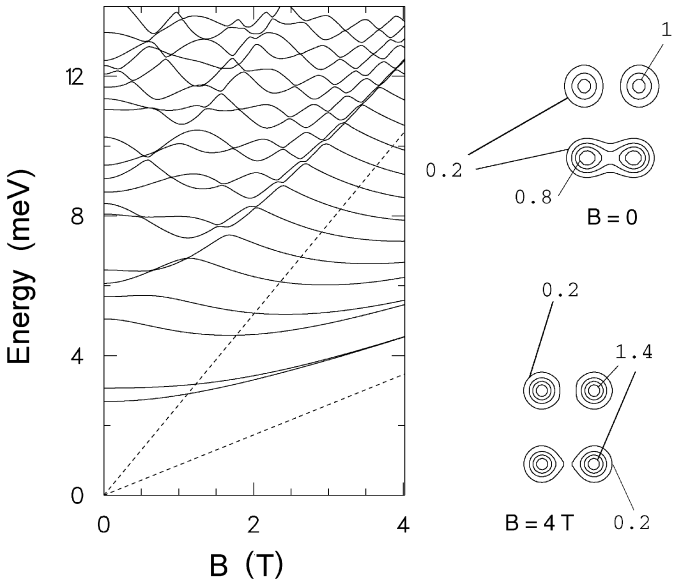

Fig. 7. SE spectrum of the $d = 70$ nm ($\hbar\omega_{y1} = \hbar\omega_{y2} = \hbar\omega_x = 3$ meV, $V_b = 2.43$ meV, $\Delta h = 0$) QDM versus B (in T). The $\hbar\Omega_c/2$ and $3\hbar\Omega_c/2$ Landau levels are given by the dashed lines. The electron densities (shown as insets) for the lowest bonding (bottom) and antibonding (top) states at $B = 0$ and $B = 4$ T illustrate the contraction of the orbitals caused by the magnetic field, which underlines the field-induced decoupling of the dots ("QDM dissociation"). Contour values are in units of 3.571×10^{-4} nm^{-2}.

Aided by the LSD calculations we construct a CIM [see e.g., Fig. 4(b)] corresponding to the SE spectrum shown in Fig. 4(a). Such SE-CIM diagrams (calibrated by corresponding LSD calculations) constructed for various QDM configurations, provide an adequate description of the spectral characteristics of QDM's [e.g., AE spectra, compare Fig. 4(b) with the corresponding LSD result for $V_b^{\rm bare} = 10$ meV shown in Fig. 5], and they may be used to guide experimental observations.

Next, we discuss briefly a generalization of the concept of quantum dots to include impurities ("dirty artificial atoms"). Addition energy spectra for the "clean" QD and for "dirty" QD's, with a hydrogenic impurity located either at the center of the dot (CI-QD) and off-center (OCI-QD) at a distance of 17.5 a_B^* from the middle, are shown in Fig. 6; in these LSD calculations we used the same bare harmonic confining frequencies as above, with the addition of the hydrogenic impurity described via a local pseudopotential [19] of core-radius 0.95 a_B^* (yielding for the ionization energy of the isolated impurity a value of 0.96 Ry*). The effect of the impurity on the effective potential for a 12-electron CI-QD is shown in the right inset to Fig. 6 along with the electron density on a line passing through the center of the dot. In the left inset to Fig. 6, we display for the $N = 12$ CI-QD the integrated electron density $n(R) = 4\pi \int_{-\infty}^{\infty} {\rm d}z \int_0^R r^2 \rho(r,z) {\rm d}r$, where r is in the plane of the dot, and the differential electron density $n'(R) = 4\pi R^2 \int_{-\infty}^{\infty} \rho(R,z) {\rm d}z$, showing that the (positively charged) hydrogenic impurity is (over) screened by two electrons which "localize" at the central region ($R \lesssim 15$ nm) about the impurity forming an "H^--defect".

Inspection of the AE spectra in Fig. 6 reveals clear signatures of shell closures at $N = 2$, 6, 12, and 20, which are the expected ones for harmonically confined free-electrons, indicating that the shell-structure maintains in the presence of electron-electron interactions and that it is rather robust to the effect of a hydrogenic impurity. We note, however, certain differences between the AE spectra of the various dots, including obliteration of the peak at $N = 2$ for the OCI-QD and the relatively less pronounced peak at $N = 6$ for the CI-QD, and significant variations in the spin-polarization patterns influenced by the hydrogenic impurity and its location in the dot.

To explore the poperties of QDM's in a magnetic field, we start first with a simple generalization of the non-interacting electrons's Darwin–Fock model [26]. The SE spectra for the QDM ($d = 70$ nm, $V_b = 2.43$ meV) in a magnetic field (B) are shown in Fig. 7 (here we neglect the Zeeman interaction which is small for our range of B values with $g^* = -0.44$ for GaAs). The main features are: (i) the multiple crossings (and avoided crossings) as B increases, (ii) the decrease of the energy gap between levels, occurring in pairs (such as the lowest bonding-antibonding pair), portraying an effective reduced coupling between the QD's comprising the QDM as B increases, (see the electron densities for $B = 0$ and $B = 4$ T in Fig. 7). and (iii) the "condensation" of the spectrum into the sequence of Landau levels $(N_L + 1/2)\hbar\Omega_c$, $N_L = 0$, 1, 2, ... , similar to the be-

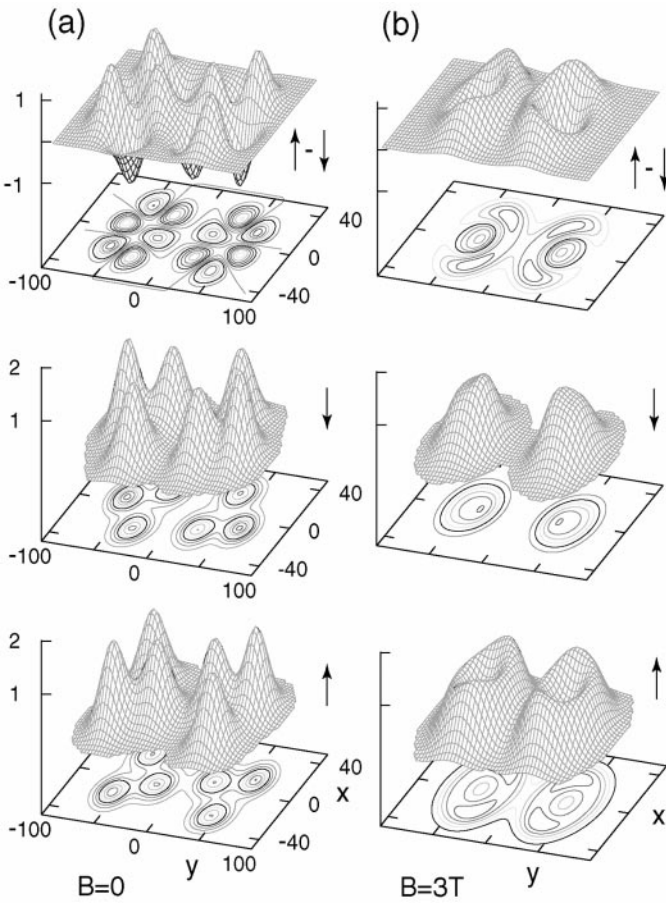

Fig. 8. sS-UHF results for a 12e QDM ($d = 70\,\text{nm}$, $V_\text{b} = 10\,\text{meV}$, $\hbar\omega_0 = 5\,\text{meV}$), without [in (a)] and with a magnetic field $B = 3\,\text{T}$ [in (b)]. For both cases, the bottom and middle panels correspond to the up-spin and down-spin electron distributions, respectively, and the top ones correspond to the difference between them (spin density). Lengths (x and y axes) in nm, density distributions (vertical axes) in $10^{-3}\,\text{nm}^{-2}$. x-axes, y-axes, and vertical-axes scales in (b) are the same as in (a).

havior of the SE Darwin–Fock spectrum for harmonically confined electrons in a circular QD [5] (note however that the geometry of the QDM is non-circular and deviates from a simple harmonic confinement).

To investigate the spectra of QDM's in a magnetic field, beyond the SE treatment, we used the spin-and-Space UHF (sS-UHF) approach [28, 34, 35]. Here the starting many-body hamiltonian is given by summing the single-paticle hamiltonian given in (1) over all N electrons and adding the term $\sum_{n<m} e^2/\kappa|\mathbf{r}_n - \mathbf{r}_m|$, where κ is the dielectric constant (for GaAs, $\kappa = 12.9$), corresponding to the interelectron Coulomb repulsion (see [28]). Before examining the magnetic-field effects on the QDM's, we recalculated their spectra, as well as those of single QD's, using the sS-UHF method, for the field-free case. On first sight, the AE's from the sS-UHF show [28] similar patterns as a function of the number of electrons (N) as those calculated by us for the same single QD's and QDM's using the LSD method (see Fig. 5). However, the spin polarizations calculated through the two methods are generally different. Furthermore, inspection of the spatial distributions of the electronic densities reveals that for the parameters used in this study the sS-UHF yielded in most cases solutions exhibiting symmetry breaking (SB) [36], i.e., solutions of lower symmetry than the symmetry of the confining potentials of the single QD's and QDM's.

An example of such broken symmetry is shown in Fig. 8(a) for the $d = 70\,\text{nm}$, $V_\text{b} = 10\,\text{meV}$ QDM (GaAs) with $\hbar\omega_x = \hbar\omega_{y1} = \hbar\omega_{y2} = \hbar\omega_0 = 5\,\text{meV}$ and $N = 12$. As evident, the electronic distributions exhibit "Wigner crystallization" (WC) [37] portrayed by 6 well-resolved humps (3 in each well) for both the up ($\uparrow$) and down ($\downarrow$) spins, and by 6 humps and 6 troughs for the spin density ($\uparrow - \downarrow$); note that the density peaks for the two spin directions do not overlap. Formation of such "Wigner supermolecules" (WSM's) in QDM's is analogous to that of "Wigner molecules" (WM's) [38] in single QD's. The mean distance between neighboring density maxima inside each of the coupled dots equals $\bar{r} \approx 20\,\text{nm}$, i.e., roughly twice larger than the effective Bohr radius $a^*_\text{B}(\kappa = 12.9) = 10.188\,\text{nm}$. Inspection of the wave functions shows that this case corresponds to an intermediate electron-density regime, where spatial localization of *individual* electrons emerges, but with finite-amplitude contributions of each of the wave functions to several of the density peaks (i.e., "weak" WM, see below); full localization into a "classical" WC requires even lower densities.

The finding of such WC is a consequence of the relatively high ratio $R_W \equiv Q/\hbar\omega_0$ (1.48 for the case in Fig. 8) between the Coulomb interaction strength Q and the parabolic confinement $\hbar\omega_0$. The Coulomb interaction strength is estimated by $Q = e^2/\kappa l_0$, where κ is the dielectric constant and $l_0 = (\hbar/m^*\omega_0)^{1/2}$ is the spatial extension of the lowest state's wave function in a parabolic confinement (here ω_0 denotes ω_x used in the above). A weakening of Q (originating from the finite thickness of the artificial QD's, which may be simulated by increasing κ), or a decrease of $\hbar\omega_0$ with increasing N (originating from Coulomb screening by the leads and gates), will affect the value of R_W. For smaller values of R_W, normal (non-crystalline) electronic spatial distributions may be recovered, while for larger values enhanced crystallization (full electron localization) toward the classical limit may be expected [28]. The failure of LSD calculations to yield such WC (both for single QD's and for QDM's [39]) is related to the self-interaction inherent to the method, i.e., while certain symmetry breaking can be obtained via LSD (e.g., "spin-density waves" [29(c)]), spatial localization of the electrons cannot be found and will require self-interaction corrections (SIC-LSD) [40].

Under the influence of an applied magnetic field, the electronic orbitals in the QDM are compressed, and the consequent increase in Coulomb repulsion drives promotion of electrons to higher orbitals of larger spatial extension. Such a process is accompanied by an increase in the spin polarization (spin flip) resulting in optimization of exchange-energy gain (such a process is analogous to that found in single QD's leading at high fields to a maximum density droplet (MDD) [6]). An example of this scenario

is shown for the QDM in Fig. 8(b) for $B = 3\,\mathrm{T}$ (the effective g^* factor was taken as $g^* = -0.44$). Here we observe that two of the down-spin electrons flipped, resulting in 8 up-spin and 4 down-spin electrons. We also observe a reduced Wigner crystallinity (partial "melting") of the WSM, portrayed by the less pronounced peaks in the electron densities [compare Fig. 8(b) with Fig. 8(a)]. Analysis of the electron densities shows enhancement in the interdot region of the QDM. Further details pertaining to the sS-UHF and the spontaneous symmetry breaking in single and molecular QD's can be found elsewhere [28]. Further studies of such broken symmetries may include: mapping of "phase-boundaries" through variations of materials dependent (e.g., dielectric constant) and externally controlled (e.g., gate voltages, interdot distances and barrier heights, and magnetic fields) parameters, and probing of excitations and spin polarizations [41].

This research is supported by the US D.O.E. (Grant No. FG05-86ER-45234), and the AFOSR.

References

1. H. Haberland (Ed.): *Clusters of Atoms and Molecules*, Springer Series in Chemical Physics **52** and **57** (Springer, Berlin 1994)
2. W.A. deHeer: Rev. Mod. Phys. **65**, 611 (1993)
3. see C. Yannouleas, U. Landman: in *Large Clusters of Atoms and Molecules*, ed. by T.P. Martin (Kluwer, Dordrecht 1996) p. 131
4. T.P. Martin: Phys. Rep. **273**, 199 (1996)
5. L.P. Kouwenhoven *et al.*: in *Mesoscopic Eletron Transport*, ed. by L.L. Sohn *et al.* (Kluwer, Dordrecht 1997) p. 105
6. R. Ashoori: Nature **379**, 413 (1996)
7. S. Tarucha: Phys. Rev. Lett. **77**, 3613 (1996)
8. U. Landman, W.D. Luedtke, N.A. Burnham, R.J. Colton: Science **248**, 454 (1990)
9. See articles in P. Serena, N. Garcia (Eds.): *Nanowires*, (Kluwer, Dordrecht 1997)
10. R.N. Barnett, U. Landman: Nature **387**, 788 (1997)
11. C. Yannouleas, U. Landman: J. Phys. Chem. B **101**, 5780 (1997); C. Yannouleas, E.N. Bogachek, U. Landman: Phys. Rev. B **57**, 4872 (1998)
12. (a) R.L. Whetten *et al.*: Adv. Mater. **5**, 428 (1996); and in W. Andreoni (Ed.): *Chemical Physics of Fullerenes 5 and 10 Years Later* (Kluwer, Dordrecht 1996) pp. 475-490; (b) C.L. Cleveland *et al.*: Z. Phys. D **40**, 503 (1997); (c) W.D. Luedtke, U. Landman: J. Phys. Chem. **100**, 13 323 (1996); *ibid*: J. Phys. Chem. B **102**, 6566 (1998); (d) C.L. Cleveland *et al.*: Phys. Rev. Lett. **79**, 1873 (1997)
13. S. Chen *et al.*: Science **280**, 2098 (1998), and references to earlier work therein
14. (a) M.M. Alvarez *et al.*: Chem. Phys. Lett. **266**, 91 (1997); (b) T.G. Schaaff *et al.*: J. Phys. Chem. B **101**, 7885 (1997)
15. C.L. Cleveland, U. Landman: J. Chem. Phys. **94**, 7376 (1991)
16. L.D. Marks: Philos. Mag. **49**, 81 (1984)
17. For a recent review, see D.M.P. Mingos: J. Chem. Soc. Dalton **5**, 561 (1996)
18. Our analysis, based on atomistic energy minimization, is essentially parameter-free and should be contrasted with multi-parameter data-fitting procedures using guessed structures including weighted distributions of cluster sizes with differing structural and morphological motifs [see e.g., W. Vogel, B. Rosner, B. Tesche: J. Phys. Chem. **97**, 11 611 (1993)]
19. N. Troullier, J.L. Martins: Phys. Rev. B **43**, 1993 (1991)
20. The core radii, in a_0, are (a tilde indicates a local component): Au: $\tilde{s}(2.50)$, $p(3.00)$, $d(2.00)$; S: $s(1.80)$, $\tilde{p}(2.30)$; C: $s(1.50)$, $\tilde{p}(1.54)$; H: $\tilde{s}(0.95)$. The Au pseudopotential is relativistic and has been weighted averaged by the j degeneracy of the $l \pm 1/2$ states [see L. Kleinman: Phys. Rev. B **21**, 2630 (1980); G.B. Bachelet, M Schlüter: Phys. Rev. B **25**, 2103 (1982)]
21. R.N. Barnett, U. Landman: Phys. Rev. B **48**, 2081 (1993)
22. D.A. Papaconstantopoulos: *Handbook of the band structure of elenental solids* (Plenum, New York 1986)
23. J.T. Khoury, R.L. Whetten: private communication
24. H. Häkkinen, R.N. Barnett, U. Landman: Phys. Rev. Lett. **82**, 3264 (1999)
25. L.P. Kouwenhoven: Science **268**, 1440 (1995); F.R. Waugh *et al.*: Phys. Rev. Lett. **75**, 705 (1995); N.C. van der Waart *et al.*: Phys. Rev. Lett. **74**, 4702 (1995); R.H. Blick *et al.*: Phys. Rev. Lett. **80**, 4032 (1998) and Phys. Rev. B **53**, 7899 (1996)
26. V. Fock: Z. Phys. **47**, 446 (1928); C.G. Darwin: Proc. Cambridge Philos. Soc. **27**, 86 (1930)
27. (a) D. Pfannkuche, V. Gudmundsson, P.A. Maksym: Phys. Rev. B **47**, 2244 (1993); (b) J.J. Palacios *et al.*: Phys. Rev. B **50**, 5760 (1994); (c) M. Fujito, A. Natori, H. Yasunaga: Phys. Rev. B **53**, 9952 (1996)
28. C. Yannouleas, U. Landman: Phys. Rev. Lett. **82**, 5325 (1999)
29. (a) M. Macucci *et al.*: Phys. Rev. B **55**, R4879 (1997); (b) I.-H. Lee *et al.*: *ibid.* **57**, 9035 (1998); (c) M. Koskinen, M. Manninen, S.M. Reimann: Phys. Rev. Lett. **79**, 1389 (1997); (d) M. Ferconi, G. Vignale: Phys. Rev. B **50**, 14 722 (1994)
30. M. Eto: Jpn. J. Appl. Phys. **36**, 3924 (1997)
31. A 3D field-free version of the TCOM has been used in the description of fission in metal clusters [C. Yannouleas, U. Landman: J. Phys. Chem. **99**, 14 577 (1995); C. Yannouleas *et al.*: Comments At. Mol. Phys. **31**, 445 (1995)] and nuclei [J. Maruhn, W. Greiner: Z. Phys. **251**, 431 (1972); C.Y. Wong: Phys. Lett. **30B**, 61 (1969)]
32. The method described in [21] was used with a 60.16 Ry^* [$\mathrm{Ry}^*(\mathrm{GaAs}) = 5.48$ meV] kinetic-energy cutoff for the plane wave basis
33. For a single 2D isotropic harmonic oscillator, peaks in AE spectra at shell closures ($N = 2$, 6, 12, 20, ...) and half-shell closures ($N = 4$, 9, 16, ...) are expected (see e.g. the QD curve in Fig. 5, although V^{eff} exhibits deviations from harmonicity). For QDM's with a sufficiently large barrier between the dots, such shell-closure effects occur at twice the single QD electron numbers, for states lying below the barrier (see e.g. $N = 4$ for QDM's with $V_{\mathrm{b}}^{\mathrm{bare}} = 10$ and 30 meV in Fig. 5).
34. Y.G. Smeyers: in R. Carbó, M. Klobukowski (Eds.): *Self-Consistent Field: Theory and Applications* (Elsevier, Amsterdam 1990) p. 80
35. Our sS-UHF employs N (mean-field) effective potentials and differs from the usual (restricted) HF in two ways: (i) it employs different orbitals for different spin directions (DODS), and (ii) it relaxes the requirement that the elec-

tron wave functions be constrained by the symmetry of the external confining field. Earlier HF studies of single QD's did not incorporate the spin-and-Space unrestrictions simultaneously. For example, Wigner molecules (at $B = 0$ and/or finite B) were not found by D. Pfannkuche *et al.*: [Phys. Rev. B **47**, 2244 (1993)] and M. Fujito *et al.*: [Phys. Rev. B **53**, 9952 (1996)]. Indeed, using symmetry-restricted variational wave functions, we have reproduced the results of these studies, while with the sS-UHF, with no such restrictions, broken-symmetry solutions with lower energy were obtained as described here. We further note here that employing a Space-UHF, but only for fully polarized single QD's (i.e., under high magnetic fields where the spin unrestriction is not at play), Wigner crystallization has been investigated [38(b)]. LSD calculations [29, 39] where there are only two effective potentials (associated with the two spin directions) cannot yield in general crystallized solutions (except for $N = 2$ in a deformed single QD and in a QDM [39]). While certain symmetry breaking can be obtained with LSD (e.g., pure spin density waves [29(c)]), spatial localization may require self-interaction corrections (SIC-LSD, see [40])

36. (a) J. Paldus in [34], p. 1; For a general discussion of SB and the associated emergence of highly degenerate manifolds of excitations (Goldstone modes) see: (b) P.W. Anderson, *Basic Notions of Condensed Matter Physics* (Benjamin, Menlo Park, CA 1984), and (c) P. Ring, P. Schuck: *The Nuclear Many-Body Problem* (Springer, New York 1980), in the context of SB in finite systems and restoration of broken symmetries (Ch. 11); (d) D.J. Thouless: Nucl. Phys. **21**, 225 (1960)
37. E. Wigner: Phys. Rev. **46**, 1002 (1934)
38. (a) P.A. Maksym: Physica B **184**, 385 (1993); (b) H.-M. Müller, S.E. Koonin: Phys. Rev. B **54**, 14 532 (1996); (c) W. Häusler: Z. Phys. B **99**, 551 (1996)
39. We remark that only in the case of $N = 2$ and for the QDM's with $V_{\rm b}^{\rm bare} = 0$, 10 and 30 meV (see description in Fig. 5), as well as for a deformed single QD, did our LSD calculation yield (singlet) localized electron states
40. J.P. Perdew, A. Zunger: Phys. Rev. B **23**, 5048 (1981); R.O. Jones, O. Gunnarsson: Rev. Mod. Phys. **61**, 689 (1989)
41. This includes spectroscopical probing of the intrinsic electronic spectra of the SB states, and of the rotational and vibrational spectra (Goldstone modes [36(b and c)]) of the symmetry broken states (WM's) using radio and/or microwave frequencies (and possibly employing polarized radiation), as well as studies of the effect of impurities on the formation of SB states and their spectra; for investigations of impurity-pinning effects, see C. Yannouleas, U. Landman, to be published